



Cite this: *J. Mater. Chem. A*, 2015, **3**, 24064

# A comparative study of $\text{SrCo}_{0.8}\text{Nb}_{0.2}\text{O}_{3-\delta}$ and $\text{SrCo}_{0.8}\text{Ta}_{0.2}\text{O}_{3-\delta}$ as low-temperature solid oxide fuel cell cathodes: effect of non-geometry factors on the oxygen reduction reaction†

Mengran Li,<sup>a</sup> Wei Zhou,<sup>\*a</sup> Vanessa K. Peterson,<sup>b</sup> Mingwen Zhao<sup>c</sup> and Zhonghua Zhu<sup>\*a</sup>

The oxygen reduction reaction (ORR) activity of cathodes has to be improved to realize the low-temperature operation of solid-oxide fuel cells (SOFCs). Whilst geometric factors are conventionally accepted to influence the ORR activity of perovskite cathodes, other factors may also contribute and therefore need to be explored. Here, we substituted 20% niobium and tantalum which have similar ionic radii into strontium cobaltites to obtain the two perovskite oxides  $\text{SrCo}_{0.8}\text{Nb}_{0.2}\text{O}_{3-\delta}$  (SCN20) and  $\text{SrCo}_{0.8}\text{Ta}_{0.2}\text{O}_{3-\delta}$  (SCT20), respectively. Our study of the isostructural SCN20 and SCT20 allows geometric effects to be separated from other factors, and we observe better cathode performance of SCT20 cathode, which may be related to the lower electronegativity of  $\text{Ta}^{5+}$ , thus resulting in higher oxygen surface exchange kinetics and diffusivity as compared with  $\text{Nb}^{5+}$ .

Received 9th September 2015  
Accepted 2nd November 2015

DOI: 10.1039/c5ta07178j

www.rsc.org/MaterialsA

## 1. Introduction

Solid-oxide fuel cells (SOFCs) are energy devices that convert various fuels into electricity with high efficiencies. Lowering the operating temperature of SOFCs is of importance and interest,<sup>1</sup> because this facilitates the use of low-cost construction materials, accelerates start-up/shutdown procedures, and improves the long-term durability of the system.<sup>2</sup> However, the polarization losses of the SOFC electrodes, especially those arising from the slow kinetics of the oxygen reduction reaction (ORR) at the cathodes still remain as the major challenge for low temperature SOFC.<sup>3–5</sup>

It is widely accepted that the ORR occurs when oxygen is absorbed and diffuses towards the triple phase boundary (TPB), where the cathode (electronic conductor), electrolyte (ionic conductor), and gaseous phase meet, followed by charge gain and diffusion into the electrolyte.<sup>6–8</sup> Therefore, the oxygen surface-exchange coefficient ( $k$ ) and oxygen bulk-diffusion coefficient ( $D$ ) are regarded as key parameters affecting the ORR, with larger values promoting a faster ORR. The parameters  $k$  and  $D$  are enhanced by high mixed ionic and electronic conductivities (MIECs).<sup>9</sup> The mixed conductivities of a cathode

will extend the active sites throughout the cathode surface, therefore enhancing the ORR.

Efforts have been devoted to develop cathode materials for low-temperature solid-oxide fuel cells (LT-SOFCs),<sup>10–18</sup> and perovskite oxides with high MIECs are regarded as one of the most promising candidates for catalyzing the ORR at low temperature.<sup>19</sup> It is well known that perovskite structures are stable to extensive compositional modification, with such strategy useful in tuning properties for target application.<sup>20</sup> Amongst the MIEC materials, perovskite-structure strontium cobaltites show high mixed conductivities,<sup>21</sup> and are therefore of great interest for application as LT-SOFC cathodes. However, the perovskite phase of strontium cobaltite is unstable at the operating temperature of SOFCs.<sup>22–24</sup> Strategic doping with high valence-state cations such as  $\text{P}^{5+}$ ,  $\text{Nb}^{5+}$  and  $\text{Sb}^{5+}$ , were found to be of benefit, *i.e.* stabilizing the perovskite structure at high temperature.<sup>25–28</sup>

Furthermore, researchers also explored the strategic design of next-generation LT-SOFC cathodes by examining approaches such as the use of the octahedral factor<sup>29</sup> or the Goldschmidt tolerance factor<sup>30,31</sup> in an effort to predict perovskite structures with favourable electrochemical activities.<sup>9,32</sup> For example, cathode performance is enhanced by disordered oxygen vacancies, increasing structural symmetry, critical radius<sup>33</sup> and lattice free volumes,<sup>32</sup> as well as lowering metal–oxygen bonding energies.<sup>9</sup> However, such factors may co-exist, and are usually affected by the crystal structural geometry. The determination of their independent contribution to cathode performance remains a challenge. To this end, geometric factors should be constrained in a study of other factors. It is well known that

<sup>a</sup>School of Chemical Engineering, University of Queensland, St. Lucia, Queensland 4072, Australia. E-mail: zhou.wei@uq.edu.au; zhu.z@uq.edu.au

<sup>b</sup>Australian Nuclear Science and Technology Organisation, Lucas Heights, NSW, 2234, Australia

<sup>c</sup>School of Physics and State Key Laboratory of Crystal Materials, Shandong University, Jinan 250100, Shandong, China

† Electronic supplementary information (ESI) available. See DOI: 10.1039/c5ta07178j

Nb<sup>5+</sup> and Ta<sup>5+</sup> share the same ionic radii (0.64 Å for both)<sup>34,35</sup> and fixed high valence-states (5+) at high temperature in an oxidizing environment, but they are different in electronegativity. The Pauling electronegativity of Nb<sup>5+</sup> (1.87) is larger than that of Ta<sup>5+</sup> (1.8).<sup>36,37</sup> Electronegativity is the tendency of an atom or group to attract electrons,<sup>38</sup> and is therefore expected to influence the electrochemical performance of SOFC cathodes.

Herein, we compared the properties of SrCo<sub>0.8</sub>Nb<sub>0.2</sub>O<sub>3-δ</sub> (SCN20) and SrCo<sub>0.8</sub>Ta<sub>0.2</sub>O<sub>3-δ</sub> (SCT20) including their crystal structures, conductivities, *k* and *D* values, as well as their ORR activities. The similar ionic radii of Nb and Ta are expected to promote similar geometry factors, enabling the contributions from non-geometry factors such as electronegativity on the ORR to be separated from that arising from geometrical factors.

## 2. Experimental

Phase-pure SCN20 and SCT20 powders were synthesized through solid-state methods. Stoichiometric mixtures of SrCoO<sub>3</sub> (≥99.9%, Aldrich), Co<sub>3</sub>O<sub>4</sub> (≥99.9%, ≤10 μm, Aldrich), and Nb<sub>2</sub>O<sub>5</sub> (≥99.9%, Aldrich) or Ta<sub>2</sub>O<sub>5</sub> (≥99.9%, Aldrich) were ball-milled for 24 h, followed by pelletizing and sintering at 1200 °C for 20 h in stagnant air.

Thermogravimetric analysis (TGA) was performed to estimate the oxygen content of SCN20 and SCT20 at different temperatures by annealing powder samples from room temperature to 850 °C at 1 °C min<sup>-1</sup>. The samples were pre-treated by pelletizing at the same pressure to ensure similar grain size and baking at 200 °C for 2 h to remove absorbed moisture. Weight changes of SCN20 and SCT20 were recorded when the flowing gas was changed from pure N<sub>2</sub> to air, and the samples were first heated at 460 °C (furnace temperature 500 °C) until the weight reach equilibrium in flowing pure N<sub>2</sub>. The initial oxygen contents of samples were obtained from the Rietveld refinement results of NPD patterns, and double checked by the titration method as described in our previous work.<sup>18</sup> The oxidation state (*Z*) changes of Co were then estimated according to the change in oxygen non-stoichiometry (*δ*):

$$Z = \frac{3 - 2\delta}{0.8}$$

Symmetrical cells for impedance studies were fabricated by nitrogen-borne spraying the cathode powders, which were suspended in isopropyl alcohol, onto both sides of a Sm<sub>0.2</sub>Ce<sub>0.8</sub>O<sub>1.9</sub> (SDC) electrolyte disk, and then calcining at 1000 °C in stagnant air for 2 h. Silver mesh was used as current collectors of the symmetrical cells, which were attached to both sides of the cell using silver paste. The samples for electrical conductivity and electrical conductivity relaxation (ECR) tests were dense bars with dimension 0.65 cm × 0.2 cm × 0.1 cm. The cathode powder was ball milled at 400 rpm for 3 h, pelletized at 400 MPa, and then sintered at 1200 °C for 10 h. Both SCN20 and SCT20 have densities >95% relative to their theoretical densities as confirmed by Archimedes method. The bars were well polished and attached with silver leads as electrodes using silver paste.

The anode-supported single cells were fabricated by co-pressing the anode and SDC electrolyte into pellets, and sintering at 1350 °C for 3 h. The anode material was prepared by ball milling commercial NiO, SDC, and dextrin pore former in a weight ratio of 6 : 4 : 1, respectively, for 24 h in ethanol. The cathode material was sprayed onto the SDC electrolyte, followed by calcination at 1000 °C for 2 h.

The ORR performance of the target cathode materials was evaluated using electrochemical impedance spectroscopy (EIS) in a symmetrical-cell configuration. The mechanism of the ORR was analysed by using LEVM software. A four-probe dc method was used for electrical conductivity measurements. The surface-exchange coefficient (*k*) and oxygen bulk-chemical diffusivity (*D*) of the cathode materials were obtained using ECR performed by recording the changes of the electrical conductivity with time after a step change in the ambient atmosphere with O<sub>2</sub> from 0.21 to 0.0998 atm. The change of the electrical conductivities against time were fitted using ECRTOL<sup>39</sup> to obtain *k* and *D*. A PGSTAT302 Autolab workstation was used for the electrochemical measurements including EIS, electrical conductivity, and ECR.

The crystal structures of the cathode materials were studied using X-ray powder diffraction (XRD) and neutron powder diffraction (NPD). X-ray photoelectron spectroscopy (XPS) was used to examine the binding energy of Co ions in the sample at room temperature. High resolution NPD data were collected using ECHIDNA<sup>40</sup> at the ANSTO with a neutron wavelength of 1.6219(2) Å, determined using the La<sup>11</sup>B<sub>6</sub> NIST standard reference material 660b. NPD data were collected from samples in a 6 mm vanadium can for 6 h over the angular range (2θ) 4 to 164°. GSAS-II<sup>41</sup> was employed to perform Rietveld analysis of the NPD data using a *Pm3m* cubic perovskite starting structure.<sup>42</sup> Scanning electron microscopy (SEM, Philips XL30) was also used to characterize the cathode microstructure.

The first-principles calculation were conducted with the Vienna ab initio simulation package (VASP)<sup>43,44</sup> using density-functional theory (DFT). Ion-electron interactions were treated using projector-augmented-wave potentials<sup>45</sup> and a generalized gradient approximation (GGA) in the form of Perdew–Burke–Ernzerhof was adopted to describe electron–electron interactions.<sup>46</sup> The GGA+*U* calculations were performed with the simplified spherically-averaged approach, where the *U*<sub>eff</sub> (*U*<sub>eff</sub> = *U* − *J*) is applied to d electrons. Electron wave functions were expanded using plane waves with an energy cut off of 520 eV. The Kohn–Sham equation was solved self-consistently with a convergence of 10<sup>-5</sup>. The stoichiometry of the simulated systems was set to SrCo<sub>0.75</sub>Nb<sub>0.25</sub>O<sub>3</sub>, SrCo<sub>0.75</sub>Ta<sub>0.25</sub>O<sub>3</sub> due to computational limits.

## 3. Results and discussions

The NPD results reveal that SCN20 and SCT20 both exhibit cubic perovskite structures in *Pm3m* space-group symmetry at room temperature, with similar lattice parameters of *a* = 3.8971(1) Å for SCN20 and *a* = 3.8978(2) Å for SCT20 (Fig. 1(a) and Table 1). Broad, small reflections were noted in the NPD data that were unindexed in *Pm3m* and these were excluded

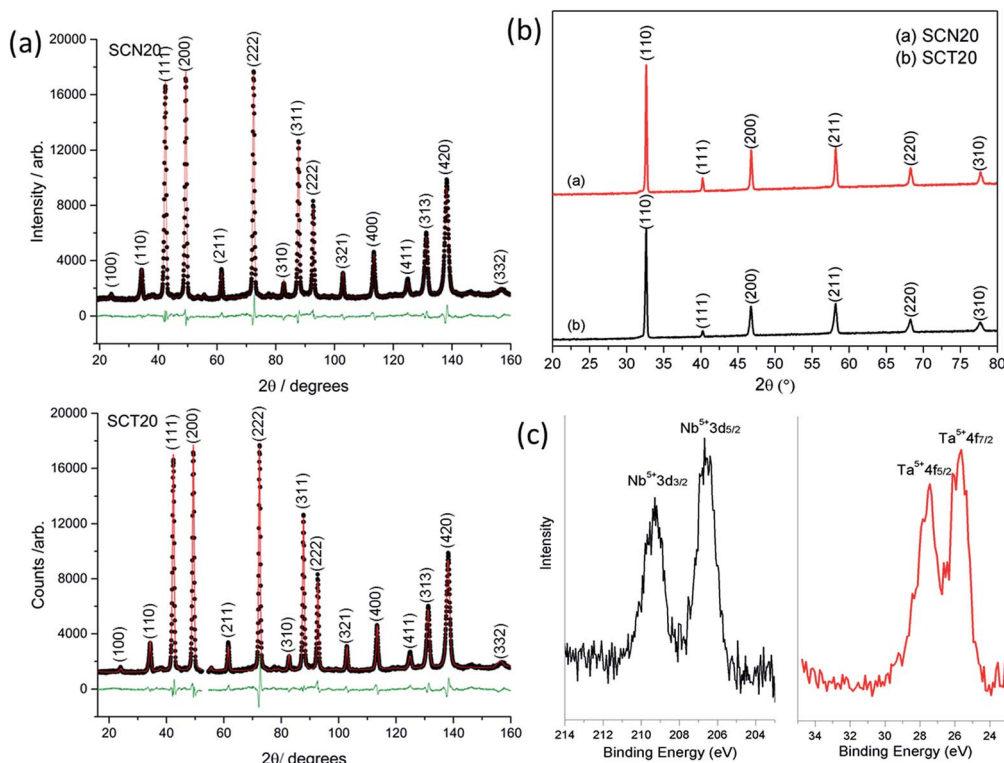


**Fig. 1** (a) Rietveld refinement plot of SCN20 (top) and SCT20 (bottom) powders at room temperature using NPD. Data are shown as black dots, the calculation as a red line, and the difference between the two as a green line. For SCN20 the weighted profile  $R$ -factor ( $R_{wp}$ ) = 4.53%, the integrated intensity  $R$ -factor ( $R_F^2$ ) = 3.46%, and goodness of fit ( $\chi^2$ ) = 2.48. For SCT20  $R_{wp}$  = 5.29%,  $R_F^2$  = 4.13%, and  $\chi^2$  = 3.42. (b) X-ray diffraction patterns of SCN20 and SCT20 at room temperature. (c) X-ray photoelectron spectroscopy profile of Nb and Ta cation in SCN20 and SCT20 respectively at room temperature.

from the structure refinement. XPS results in Fig. 1(c) shows that the binding energy (B.E.) of Nb  $3d_{5/2}$  (206.69 eV) can be assigned to  $Nb^{5+}$  [ref. 47], and B.E. of Ta  $4f_{7/2}$  (25.64 eV) to  $Ta^{5+}$  [ref. 48], indicating the same 5+ charge on both Nb and Ta cations in SCN20 and SCT20 respectively. The isostructural nature of the SCN20 and SCT20 is expected, given the similar ionic radii of  $Nb^{5+}$  and  $Ta^{5+}$ , which ensured similar-sized unit-cells. NPD results indicate a refined oxygen-stoichiometry ( $3 - \delta$ ) of SCN20 of 2.898(18), which is higher than that obtained for SCT20 of 2.843(15). The average valence state of cobalt in both samples can be obtained according to the charge balance: the average oxidation-state of cobalt cations in SCN20 is +3.44(6), which is larger overall but the same within 1 estimated standard

deviation of the +3.33(6) for SCT20. Considering the similar lattice geometries and doping level of SCT20 and SCN20, the different cobalt oxidation-state may be explained by the different electronegativity of the dopants. A dopant with higher electronegativity will draw electron density from neighbouring cobalt, resulting in increased positive charge on the cobalt. Given the higher electronegativity of  $Nb^{5+}$  than  $Ta^{5+}$ , it is understandable that the average cobalt oxidation-state is slightly higher in SCN20 in comparison to SCT20.

Further, we studied the atomic-orbital-resolved electron density of states (PDOS) projected onto the Co close to Nb or Ta through first-principles calculations. From the PDOS results (Fig. S1†), Co-PDOS peak broadening is noticeable in SCT20

**Table 1** Crystallographic details of SCN20 and SCT20 obtained from Rietveld refinement using NPD data at room temperature

Samples	$Pm\bar{3}m$ space group lattice parameter (Å)	Atom	Site	x	y	z	Occupancy
SCN20	3.8971(1)	Sr	1b	0.5	0.5	0.5	1.000
		Co	1a	0	0	0	0.79(1)
		Nb	1a	0	0	0	0.215(9)
		O	3d	0.5	0	0	0.966(6)
SCT20	3.8978(2)	Sr	1b	0.5	0.5	0.5	1.000
		Co	1a	0	0	0	0.79(1)
		Ta	1a	0	0	0	0.21(1)
		O	3d	0.5	0	0	0.947(5)

relative to SCN20, suggesting a weaker localisation of Co d states or less ionic character of Co in SCT20 than that in SCN20.<sup>49,50</sup> Therefore, the Co surrounding Ta presents slightly lower charge, which leads to a higher level of oxygen vacancy as compared with Nb. Similar Co-PDOS peak broadening also occurs in  $\text{Ba}_{0.5}\text{Sr}_{0.5}\text{Co}_{0.8}\text{Fe}_{0.2}\text{O}_{3-\delta}$  with relatively more oxygen vacancies,<sup>51</sup> further confirming that the higher oxygen vacancy level in SCT20 is related to the relatively lower charge of neighbouring Co because of Ta's lower electronegativity.

TGA was conducted to study the oxygen vacancy content ( $\delta$ ) in SCN20 and SCT20 at different temperatures in flowing air, based on the room-temperature oxygen vacancy content derived from the NPD results. The initial oxygen vacancy contents ( $\delta$ ), calculated from the Rietveld refinement results of NPD in Table 1, are around 0.102 in SCN20 and 0.157 in SCT20. While the  $\delta$  values from titration method also confirms a lower oxygen vacancy level of SCN20 (0.14) than SCT20 (0.17). Fig. 2(a) shows that both samples keep decreasing in mass with increasing temperature. These weight losses mainly stem from oxygen release, so the oxygen vacancy contents in both samples increase with temperature. More vacancies are observed in SCT20 than SCN20 at the same temperature. In addition, SCN20 decreases its weight slightly faster at temperature over ca. 780 °C, implying that it is a little easier for SCN20 to form oxygen vacancies at high temperature.

Because  $\text{Nb}^{5+}$  and  $\text{Ta}^{5+}$  have fixed oxidation states, the intake or release of oxygen strongly relies on the change of the Co oxidation state. The Co oxidation states are therefore monitored to estimate how quickly the cobalt responds to the change of

oxygen pressure. Both SCN20 and SCT20 powders were prepared for TGA by pressing and crushing in a procedure ensuring similar grain sizes (Fig. S2†) and BET surface area ( $1.038 \text{ m}^2 \text{ g}^{-1}$  for SCT20 and  $1.186 \text{ m}^2 \text{ g}^{-1}$  for SCN20). It is observed from Fig. 2(b) that Co takes a shorter time ( $\sim 4.9$  min) in SCT20 to reach equilibrium than in SCN20 ( $\sim 7.5$  min). The quicker response of Co in SCT20 implies a faster oxygen surface-exchange process compared with SCN20.

The oxygen surface-exchange coefficient ( $k$ ) and the bulk-chemical diffusivity ( $D$ ) are key factors affecting the catalytic activity of a cathode to reduce oxygen. Electrical conductivity relaxation (ECR) was performed to study these two parameters as a function of temperature. Fig. 3 compares  $k$  and  $D$  of SCN20 and SCT20. We note that oxygen diffuses slightly faster in bulk SCT20 than in SCN20. Further, SCT20 exhibits a higher activity in terms of the surface exchange of oxygen and has a lower activation energy than SCN20, resulting in a higher level surface-exchange coefficient at lower temperature. The faster oxygen intake of SCT20 than SCN20 at low temperature (462 °C) as discussed in Fig. 2(b) is consistent with this observation.

Given the similar geometries and electrical conductivities of SCN20 and SCT20 (Fig. S3†), it is likely that the higher oxygen surface-exchange rate for SCT20 mainly result from the lower electronegativity of the tantalum, leading to increased oxygen vacancies.

To the best of our knowledge, studies on the effects of electronegativity on the ORR at room temperature have been very limited. Enhanced oxygen chemisorption onto ORR catalysts was achieved by Yang *et al.*<sup>52</sup> by doping boron with low electronegativity, into carbon nanotubes. The increased positive

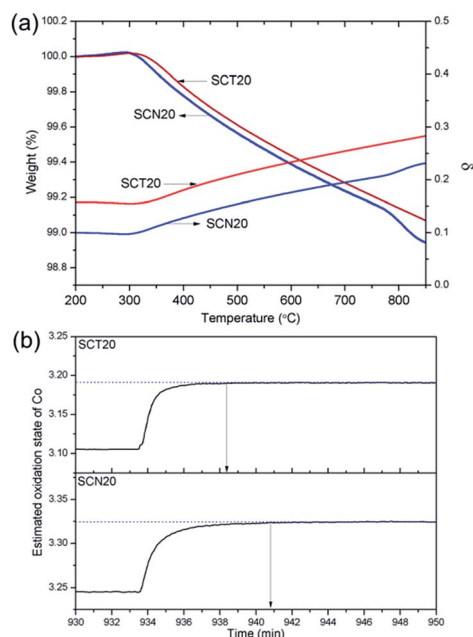


Fig. 2 (a) Weight change (obtained from TGA) and oxygen vacancy content ( $\delta$ ) of SCN20 and SCT20 powders with temperature using a ramp rate of  $1^\circ\text{C min}^{-1}$  and 2 h hold at 200 °C. (b) Change in the estimated oxidation-state of Co with time on exposure to pure  $\text{N}_2$ , then air, at 462 °C. Approximately 4.9 min is taken for the oxidation state of Co to reach equilibrium in SCT20 and 7.5 min in SCN20.

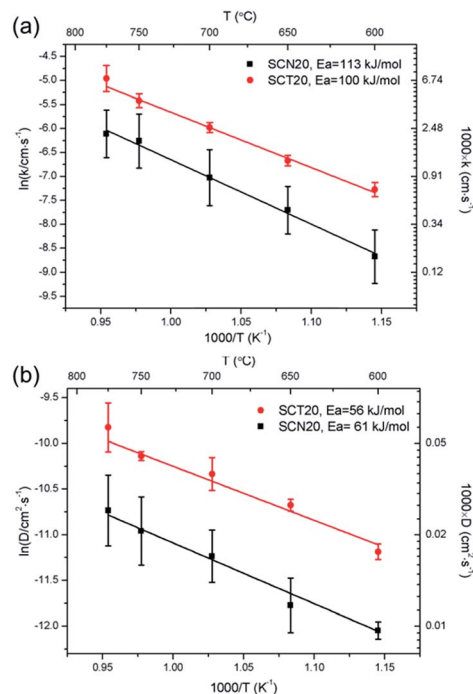


Fig. 3 SCN20 and SCT20 (a) oxygen surface-exchange coefficient ( $k$ ) and (b) oxygen diffusivity ( $D$ ) as a function of temperature obtained from ECR.



charge on boron was thought to play a significant role in the capture of oxygen. According to the electronegativity theory of Sanderson,<sup>53</sup> the effective electronegativity of atoms is equal to the geometric mean of the initial atom electronegativity due to electron distribution. Therefore, the global electronegativity of SCN20 will be slightly higher than that of SCT20. Low electronegativity leads to a decrease in work function, which significantly affects charge exchange and represents a barrier for adding or removing electrons in a solid.<sup>54</sup> Therefore, the process of charge exchange with oxygen during the oxygen surface-exchange reaction is probably improved as a result of the relatively-lower level work function in SCT20. Of more significance to the ORR is the higher level of oxygen vacancies that arises from the lower-electronegativity of tantalum. To the best of our knowledge, electronegativity has never been considered to be a factor that may influence the concentrations of oxygen vacancies in perovskite oxides. Fig. S6† further shows that SCT20 has a higher ionic conductivity than SCN20, with such difference increasing at lower temperature. The higher ionic conductivity of SCT20 arises from the higher oxygen vacancy content, which may be attributed to the lower electronegativity.

The ORR electrochemical activities of SCN20 and SCT20 were investigated using EIS in symmetrical cells with SDC electrolyte. The area-specific resistance (ASR), derived from the impedance spectra, is the key variable characterizing the cathode performance, and a low ASR results in a high ORR activity. Fig. 4 presents the ASR of SCN20 and SCT20 as a function of temperature between 500 and 700 °C. The ASR of SCT20 is lower than SCN20, being 0.092–0.097  $\Omega \text{ cm}^2$  and 0.21–0.24  $\Omega \text{ cm}^2$  at 550 °C, respectively. The lower ASR of SCT20 implies that the SCT20 cathode is more favourable for catalyzing the ORR. Additionally, SCT20 cathodes also exhibit a lower activation energy (104 kJ mol<sup>-1</sup>) for the ORR than SCN20 (118 kJ mol<sup>-1</sup>).

Given the similar microstructures as indicated by SEM (Fig. 5) and good compatibility with electrolyte (Fig. S4†) of the two cathodes, the better ORR performance of SCT20 is likely attributable to the higher oxygen surface-exchange coefficient and faster bulk-oxygen diffusion. It is likely that the low

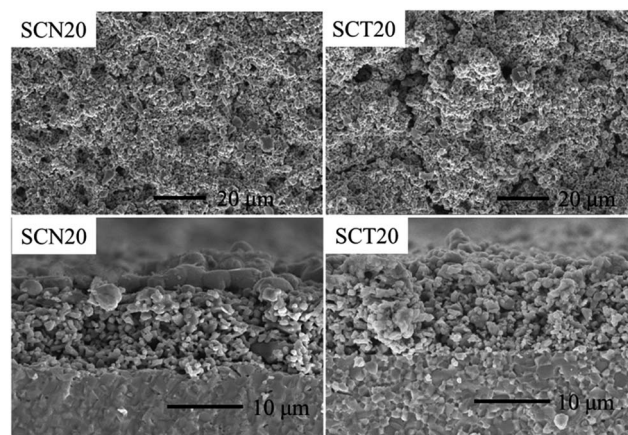


Fig. 5 Scanning electron microscope (SEM) images of topography and cross sections of SCN20 and SCT20 cathodes in a configuration of symmetrical cell.

electronegativity plays an important role in improving the ORR activity in the case of SCT20 and SCN20.

Impedance spectra of SCN20 and SCT20 were fitted to an equivalent circuit involving two processes: charge transfer and non-charge transfer (Fig. S7–S11†). The resistance of SCT20

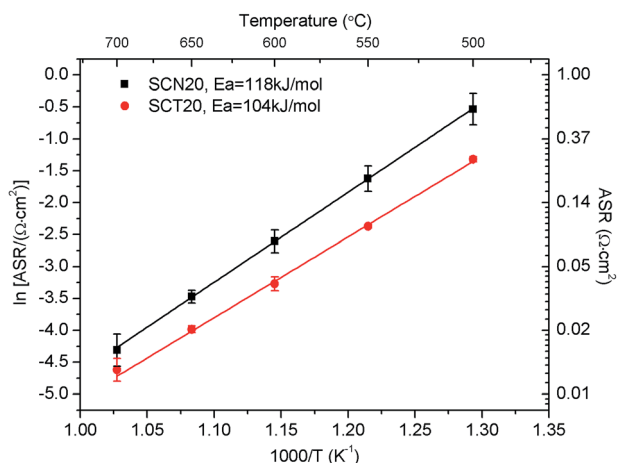


Fig. 4 Average area-specific resistance (ASR) of SCN20 and SCT20 within a cathode|SDC|cathode symmetrical cell in flowing air.

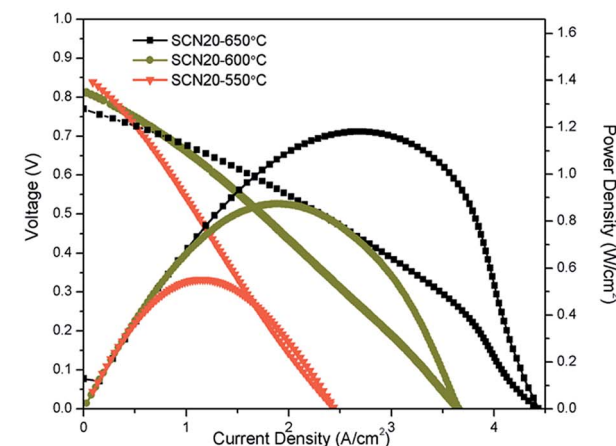
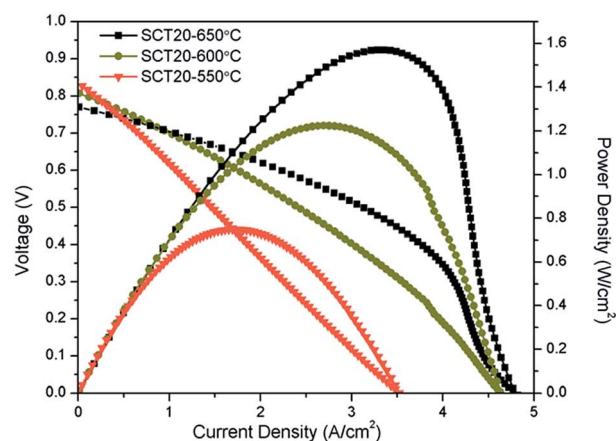


Fig. 6 The power densities of anode-supported single cell with SCN20 and SCT20 as cathode respectively.

corresponding to these processes are both lower than those of SCN20 (Table S1†). The lower ASR of both processes in SCT20 compared with SCN20 indicates that low global electronegativity can significantly improve both charge transfer and non-charge transfer processes in the ORR. The observed improvement can be reconciled with the relatively-lower work functions of SCT20 as a result of lower global electronegativity.

Accordingly, single-cell performance tests (Fig. 6) show a peak power density of  $\sim 1.22 \text{ W cm}^{-2}$  for SCT20 at  $600^\circ\text{C}$ , higher than that of  $\sim 0.95 \text{ W cm}^{-2}$  for SCN20. The better performance is a result of the higher ORR activity of SCT20 when compared with SCN20 as cathodes of the single cells.

## 4. Conclusions

The effects of non-geometry factors on the ORR activity of cathodes for SOFCs was investigated by comparing the SCN20 and SCT20 materials, where the two different dopants ( $\text{Nb}^{5+}$  and  $\text{Ta}^{5+}$ ) share similar ionic radii but different electronegativity. Given the similar lattice geometries of the two materials, the lower electronegativity of  $\text{Ta}^{5+}$  in comparison to  $\text{Nb}^{5+}$  is revealed to induce a slightly lower valence of cobalt, resulting in a higher concentration of oxygen vacancies. Lower global electronegativity is also suggested to reduce the work function of the sample, enhancing the charge-transfer processes during the oxygen surface-exchange process. As a result, SCT20 was found to have a better ORR performance than SCN20 at lower temperature as SOFC cathode. Our findings indicate that electronegativity is another factor besides geometry affecting the ORR activity of the perovskite materials, and provide new effective strategies to design novel high-performance MIEC materials.

## Acknowledgements

The authors appreciate the technical support from Centre for Microscopy and Microanalysis at the University of Queensland. This work is financially supported by Australian Research Council (DP130102151) and author Mengran Li acknowledges additional financial support from the top-up assistance program (TUAP) scholarship and the scholarship from China Scholarship Council.

## References

- 1 E. D. Wachsman and K. T. Lee, *Science*, 2011, **334**, 935–939.
- 2 N. Q. Minh, *J. Am. Ceram. Soc.*, 1993, **76**, 563–588.
- 3 B. C. Steele and A. Heinzl, *Nature*, 2001, **414**, 345–352.
- 4 A. J. Jacobson, *Chem. Mater.*, 2010, **22**, 660–674.
- 5 A. Orera and P. Slater, *Chem. Mater.*, 2010, **22**, 675–690.
- 6 S. B. Adler, *Chem. Rev.*, 2004, **104**, 4791–4844.
- 7 J.-H. Wang, M. Liu and M. Lin, *Solid State Ionics*, 2006, **177**, 939–947.
- 8 S. Yoo, A. Jun, Y.-W. Ju, D. Odkhuu, J. Hyodo, H. Y. Jeong, N. Park, J. Shin, T. Ishihara and G. Kim, *Angew. Chem., Int. Ed.*, 2014, **53**, 13064–13067.
- 9 J. Richter, P. Holtappels, T. Graule, T. Nakamura and L. Gauckler, *Monatsh. Chem.*, 2009, **140**, 985–999.
- 10 W. Zhou, Z. Shao, R. Ran, W. Jin and N. Xu, *Chem. Commun.*, 2008, 5791–5793.
- 11 W. Zhou, J. Sunarso, M. Zhao, F. Liang, T. Klande and A. Feldhoff, *Angew. Chem., Int. Ed.*, 2013, **52**, 14036–14040.
- 12 J. G. Lee, J. H. Park and Y. G. Shul, *Nat. Commun.*, 2014, **5**, 4050.
- 13 Z. Shao and S. M. Haile, *Nature*, 2004, **431**, 170–173.
- 14 S. Choi, S. Yoo, J. Kim, S. Park, A. Jun, S. Sengodan, J. Kim, J. Shin, H. Y. Jeong and Y. Choi, *Sci. Rep.*, 2013, **3**, 2426.
- 15 S. P. Simner, J. F. Bonnett, N. L. Canfield, K. D. Meinhardt, J. P. Shelton, V. L. Sprenkle and J. W. Stevenson, *J. Power Sources*, 2003, **113**, 1–10.
- 16 X. Zhang, L. Liu, Z. Zhao, B. Tu, D. Ou, D. Cui, X. Wei, X. Chen and M. Cheng, *Nano Lett.*, 2015, **15**, 1703–1709.
- 17 Y. Zhu, J. Sunarso, W. Zhou, S. Jiang and Z. Shao, *J. Mater. Chem. A*, 2014, **2**, 15454–15462.
- 18 M. Li, W. Zhou and Z. Zhu, *ChemElectroChem*, 2015, **2**, 1331–1338.
- 19 W. Zhou, R. Ran and Z. Shao, *J. Power Sources*, 2009, **192**, 231–246.
- 20 M. Pena and J. Fierro, *Chem. Rev.*, 2001, **101**, 1981–2018.
- 21 V. Kharton, A. Yaremchenko, A. Kovalevsky, A. Viskup, E. Naumovich and P. Kerko, *J. Membr. Sci.*, 1999, **163**, 307–317.
- 22 Z. Deng, W. Yang, W. Liu and C. Chen, *J. Solid State Chem.*, 2006, **179**, 362–369.
- 23 J. Rodriguez, J. Gonzalez-Calbet, J. Grenier, J. Pannetier and M. Anne, *Solid State Commun.*, 1987, **62**, 231–234.
- 24 J. Rodriguez and J. Gonzalez-Calbet, *Mater. Res. Bull.*, 1986, **21**, 429–439.
- 25 A. Aguadero, J. A. Alonso, D. Pérez-Coll, C. de la Calle, M. a. T. Fernández-Díaz and J. B. Goodenough, *Chem. Mater.*, 2010, **22**, 789–798.
- 26 C. A. Hancock, R. C. T. Slade, J. R. Varcoe and P. R. Slater, *J. Solid State Chem.*, 2011, **184**, 2972–2977.
- 27 M. Li, W. Zhou, X. Xu and Z. Zhu, *J. Mater. Chem. A*, 2013, **1**, 13632–13639.
- 28 W. Zhou, W. Q. Jin, Z. H. Zhu and Z. P. Shao, *Int. J. Hydrogen Energy*, 2010, **35**, 1356–1366.
- 29 C. Li, K. C. K. Soh and P. Wu, *J. Alloys Compd.*, 2004, **372**, 40–48.
- 30 O. Muller and R. Roy, *The major ternary structural families*, Springer-Verlag, New York, 1974.
- 31 N. P. Vyshatko, V. Kharton, A. L. Shaula, E. N. Naumovich and F. M. B. Marques, *Mater. Res. Bull.*, 2003, **38**, 185–193.
- 32 A. F. Sammells, R. L. Cook, J. H. White, J. J. Osborne and R. C. MacDuff, *Solid State Ionics*, 1992, **52**, 111–123.
- 33 J. Kilner and R. Brook, *Solid State Ionics*, 1982, **6**, 237–252.
- 34 R. t. Shannon and C. T. Prewitt, *Acta Crystallogr., Sect. B: Struct. Crystallogr. Cryst. Chem.*, 1969, **25**, 925–946.
- 35 R. t. Shannon and C. Prewitt, *Acta Crystallogr., Sect. B: Struct. Crystallogr. Cryst. Chem.*, 1970, **26**, 1046–1048.
- 36 C. K. Jørgensen, in *Progress in Inorganic Chemistry*, John Wiley & Sons, Inc., 2007, pp. 101–158.
- 37 S. F. Matar, G. Campet and M. A. Subramanian, *Prog. Solid State Chem.*, 2011, **39**, 70–95.

- 38 R. G. Parr, R. A. Donnelly, M. Levy and W. E. Palke, *J. Chem. Phys.*, 1978, **68**, 3801–3807.
- 39 F. Ciucci, *Solid State Ionics*, 2013, **239**, 28–40.
- 40 K.-D. Liss, B. Hunter, M. Hagen, T. Noakes and S. Kennedy, *Phys. B*, 2006, **385**, 1010–1012.
- 41 B. H. Toby and R. B. von Dreele, *J. Appl. Crystallogr.*, 2013, **46**, 544–549.
- 42 A. Aguadero, C. d. l. Calle, J. A. Alonso, M. J. Escudero, M. T. Fernández-Díaz and L. Daza, *Chem. Mater.*, 2007, **19**, 6437–6444.
- 43 G. Kresse and J. Hafner, *Phys. Rev. B: Condens. Matter Mater. Phys.*, 1993, **47**, 558–561.
- 44 G. Kresse and J. Furthmüller, *Phys. Rev. B: Condens. Matter Mater. Phys.*, 1996, **54**, 11169–11186.
- 45 G. Kresse and D. Joubert, *Phys. Rev. B: Condens. Matter Mater. Phys.*, 1999, **59**, 1758–1775.
- 46 J. P. Perdew, K. Burke and M. Ernzerhof, *Phys. Rev. Lett.*, 1996, **77**, 3865–3868.
- 47 G. E. McGuire, G. K. Schweitzer and T. A. Carlson, *Inorg. Chem.*, 1973, **12**, 2450–2453.
- 48 S. F. Ho, S. Contarini and J. W. Rabalais, *J. Phys. Chem.*, 1987, **91**, 4779–4788.
- 49 M. Ramos, M. N. Batista, A. Martínez and H. F. Busnengo, in *Dynamics of Gas-Surface Interactions*, ed. R. Díez Muiño and H. F. Busnengo, Springer Berlin Heidelberg, 2013, pp. 131–155.
- 50 U. G. Singh, J. Li, J. W. Bennett, A. M. Rappe, R. Seshadri and S. L. Scott, *J. Catal.*, 2007, **249**, 349–358.
- 51 E. A. Kotomin, Y. A. Mastrikov, M. M. Kuklja, R. Merkle, A. Roytburd and J. Maier, *Solid State Ionics*, 2011, **188**, 1–5.
- 52 L. Yang, S. Jiang, Y. Zhao, L. Zhu, S. Chen, X. Wang, Q. Wu, J. Ma, Y. Ma and Z. Hu, *Angew. Chem.*, 2011, **123**, 7270–7273.
- 53 R. T. Sanderson, *J. Am. Chem. Soc.*, 1983, **105**, 2259–2261.
- 54 M. T. Greiner, L. Chai, M. G. Helander, W.-M. Tang and Z.-H. Lu, *Adv. Funct. Mater.*, 2012, **22**, 4557–4568.